Communications in Theoretical Physics

Commun. Theor. Phys. **78** (2026) 025301 (9pp) https://doi.org/10.1088/1572-9494/adfdc1
CSTR: 32041.14.CTPadfdc1

Ab initio calculations of isomers in nuclei near the magic number $N = 50$

S Q Fan[1], Q Yuan[2], R Z Hu[1], S L Jin[1], J H Hou[1] and F R Xu[1,2,*]

[1] School of Physics, and State Key Laboratory of Nuclear Physics and Technology, Peking University, Beijing 100871, China
[2] Southern Center for Nuclear-Science Theory (SCNT), Institute of Modern Physics, Chinese Academy of Sciences, Huizhou 516000, China

E-mail: frxu@pku.edu.cn

Received 9 May 2025, revised 10 July 2025
Accepted for publication 21 August 2025
Published 26 September 2025

Abstract

The study of nuclear isomers can deepen our understanding of nuclear structure and astrophysics. In this work, we have performed the *ab initio* calculations of isomers in the $N = 49$ isotones. With a chiral two- plus three-nucleon force, the valence-space effective Hamiltonian was derived using the *ab initio* many-body perturbation theory named $\hat{Q}$-box folded diagrams. The effective operators of electromagnetic operators and β-decay were obtained using $\hat{\Theta}$-box folded diagrams. With the effective Hamiltonian and operators, we studied the properties of the isomers, gaining a microscopic understanding of the single-particle behaviour of the isomers which we are interested in, showing the reliability of the *ab initio* calculations.

Keywords: *Ab initio* calculations, isomerism, chiral two- plus three-nucleon force, beta decay, electromagnetic transitions

(Some figures may appear in colour only in the online journal)

1. Introduction

Nuclear isomers, defined as metastable excited states of atomic nuclei, provide us with some unique opportunities for advancing our understanding of nuclear physics and astrophysics [1]. These long-lived excited states have attracted considerable research interest [2] over the past two decades due to their distinctive quantum mechanical properties and potential applications. Among various types of nuclear isomers, spin isomers, which arise from the difficulty in meeting spin selection rules, represent one of the most prevalent and extensively studied categories. The investigation of spin isomers holds particular significance in elucidating the fundamental properties of atomic nuclei, as well as promoting the development of nuclear experimental techniques.

Nuclei in the vicinity of the neutron number $N = 50$ and the proton number $Z = 40$ exhibit a remarkable abundance of spin isomers, presenting a fertile ground for nuclear structure studies. These isomeric states predominantly originate from either single-hole excitation from $\nu 0g_{9/2}$ to $\nu 1p_{1/2}$ or single-particle excitation from $\pi 1p_{1/2}$ to $\pi 0g_{9/2}$. The large differences in angular momentum ($\Delta j = 4$) between the first-excited state and the ground state create favorable conditions for the formation of long-lived isomeric states. The systematic investigation of spin isomers in this mass region can provide insights into both the underlying mechanisms of spin isomers and the shell structure properties around the double-closed-shell nucleus ^{90}Zr.

While phenomenological theoretical approaches have been extensively employed to investigate spin isomers, the application of *ab initio* theoretical frameworks to isomeric state calculations remains rarely explored. The nuclear *ab initio* theory, which aims to solve the nuclear many-body problem from first principle using realistic nuclear interactions, represents the forefront of contemporary nuclear theoretical frameworks, offers the potential for parameter-free predictions of nuclear properties and could provide novel insights into the microscopic origins of isomers. Over the past two decades, remarkable advances have been achieved in *ab initio* many-body methods [3–6] with nuclear forces

* Author to whom any correspondence should be addressed.

based on chiral effective field theory [7]. These developments have significantly expanded the reach of *ab initio* calculations to medium-mass nuclei, enabling the theoretical investigation of complex nuclear phenomena. The systematic uncertainties inherited in these calculations can now be quantified through order-by-order improvements in the chiral expansion, providing a rigorous framework for assessing theoretical predictions of nuclear observables, including spectroscopic properties relevant to isomeric states.

In the present work, we employ the *ab initio* many-body perturbation theory (MBPT) [8], which is one of the most powerful *ab initio* many-body methods, to systematically study the $1/2^-$ spin isomer in the $N = 49$ isotones, including ^{83}Se, ^{85}Kr, ^{87}Sr, ^{89}Zr, ^{91}Mo and ^{93}Ru. The systematic study of isotones offers a unique probe to examine the evolution of single-particle properties, the robustness of shell closure and the microscopic mechanisms governing isomer formation. By analyzing these systems from an *ab initio* perspective, we can gain deeper insights into the influence of single-hole excitation on spin isomers in this mass region. Moreover, we use MBPT to study the decay properties, including $M4$ magnetic transitions and β decay, of these isomers consistently, giving good results.

2. Theory

2.1. Ab initio many-body perturbation theory

The intrinsic Hamiltonian of an A-nucleon system can be written as

$$H = \sum_{i=1}^{A}\left(1 - \frac{1}{A}\right)\frac{\boldsymbol{p}_i^2}{2m} + \sum_{i<j}^{A}\left(v_{ij}^{\mathrm{NN}} - \frac{\boldsymbol{p}_i \cdot \boldsymbol{p}_j}{mA}\right) + \sum_{i<j<k}^{A} v_{ijk}^{\mathrm{3N}}, \tag{1}$$

where $\boldsymbol{p}_i$ and $\boldsymbol{p}_j$ are the nucleon momentum in the laboratory, m means the mass of the nucleon, and v_{ij}^{NN} and v_{ijk}^{3N} are the nucleon-nucleon (NN) and three-nucleon (3N) interactions, respectively. Due to the large cost of full inclusion of three-nucleon force (3NF) during ab initio many-body calculations, the normal-ordered two-body (NO2B) approximation [9] has been widely used in nuclear ab initio calculations to reduce the calculational cost. To do this, we first performed the Hartree–Fock (HF) calculation of the initial Hamiltonian (1) in harmonic-oscillator (HO) basis, getting the HF basis. Then, we transferred the Hamiltonian (1) to the HF basis, and normal ordered it with respect to the HF reference state [10].

In this work, we used the *ab initio* MBPT [8] to construct the realistic valence-space effective Hamiltonian and other effective operators consistently for shell-model (SM) calculation. To do this, we separated the normal-ordered Hamiltonian into the one-body part H_0 and the perturbative part H_1 [11, 12]. The realistic valence-space effective interaction matrix elements for SM calculation was obtained by the so-called $\hat{Q}$-box folded diagrams [13]. Due to the non-degenerate property of the HF states, the extended Kuo–Krenciglowa method [14, 15] was used to build the effective Hamiltonian H_{eff}. With the valence-space and its complementary-space projection operators P and Q, we iteratively solve the equation

$$H_{\mathrm{eff}}^{(\kappa)} = PH_0P + \hat{Q}(\epsilon) + \sum_{n=1}^{\infty}\frac{1}{n!}\frac{\mathrm{d}^n\hat{Q}(\epsilon)}{\mathrm{d}\epsilon^n}\{H_{\mathrm{eff}}^{(\kappa-1)} - \epsilon\}^n, \tag{2}$$

with κ being the κ-th iteration and the starting energy ϵ. The definition of $\hat{Q}$ box is

$$\hat{Q}(\epsilon) = PH_1P + PH_1Q\frac{1}{\epsilon - QHQ}QH_1P, \tag{3}$$

with its derivatives

$$\hat{Q}_n(\epsilon) = \frac{1}{n!}\frac{\mathrm{d}^n\hat{Q}(\epsilon)}{\mathrm{d}\epsilon^n}. \tag{4}$$

The realistic valence-space single-particle energies are obtained by the so-called $\hat{S}$-box folded diagrams [16], which is defined as the one-body part of $\hat{Q}$ box. Both the $\hat{S}$ box and $\hat{Q}$ box are calculated up to the third order in this work.

To calculate other observables of nuclei, we used the so-called $\hat{\Theta}$ box [8] to renormalize the full-space operator Θ into the valence-space, getting the valence-space effective operator Θ_{eff}. The $\hat{\Theta}$ box and their definition are defined as [8, 17]

$$\hat{\Theta}(\epsilon) = P\Theta P + P\Theta Q\frac{1}{\epsilon - QHQ}QH_1P, \tag{5}$$

$$\hat{\Theta}(\epsilon_1;\,\epsilon_2) = PH_1Q\frac{1}{\epsilon_1 - QHQ}Q\Theta Q\frac{1}{\epsilon_2 - QHQ}QH_1P, \tag{6}$$

and

$$\hat{\Theta}_n = \frac{1}{n!}\frac{\mathrm{d}^n\hat{\Theta}(\epsilon)}{\mathrm{d}\epsilon^n}, \tag{7}$$

$$\hat{\Theta}_{mn} = \frac{1}{m!n!}\frac{\mathrm{d}^m}{\mathrm{d}\epsilon_1^m}\frac{\mathrm{d}^n}{\mathrm{d}\epsilon_2^n}\hat{\Theta}(\epsilon_1;\,\epsilon_2)\Big|_{\epsilon_1=\epsilon_2=\epsilon}. \tag{8}$$

The valence-space effective operator Θ_{eff} is defined as

$$\Theta_{\mathrm{eff}} = \sum_{\gamma,\eta}|\psi_\gamma\rangle\langle\tilde{\Psi}_\gamma|\Theta|\Psi_\eta\rangle\langle\tilde{\psi}_\eta|, \tag{9}$$

where $|\Psi_\gamma\rangle$ means the full-space wave-function and $|\psi_\gamma\rangle = P|\Psi_\gamma\rangle$ is the valence-space wave-function. With the $\hat{Q}$ box and $\hat{\Theta}$ box, the effective operator Θ_{eff} can then be written as,

$$\Theta_{\mathrm{eff}} = H_{\mathrm{eff}}\hat{Q}^{-1}\left(\sum_i^{\infty}\chi_i\right), \tag{10}$$

where

$$\begin{aligned}
\chi_0 &= (\hat{\Theta}_0 + \mathrm{h.c.}) + \hat{\Theta}_{00}\\
\chi_1 &= (\hat{\Theta}_1\hat{Q} + \mathrm{h.c.}) + (\hat{\Theta}_{01}\hat{Q} + \mathrm{h.c.})\\
\chi_2 &= (\hat{\Theta}_1\hat{Q}_1\hat{Q} + \mathrm{h.c.}) + (\hat{\Theta}_2\hat{Q}\hat{Q} + \mathrm{h.c.})\\
&\quad + (\hat{\Theta}_{02}\hat{Q}\hat{Q} + \mathrm{h.c.}) + \hat{Q}\hat{\Theta}_{11}\hat{Q}.\\
&\quad \cdots
\end{aligned} \tag{11}$$

In this work, we truncated the χ_i series at $i = 2$, which is sufficient for the convergence [8]. To be consistent with the H_{eff}, the $\hat{\Theta}$ box were also calculated up to the third order.

2.2. Other operators

In the present work, we focused on the magnetic operator and Gamow–Teller β decay. In this subsection, we briefly introduce the basic equations and concepts of these operators. A more systematic introduction of these operators can be found in [18].

2.2.1. Magnetic operator. The tensor component of the full-space bare magnetic transition tensor operator $\boldsymbol{M}\lambda$ is given by [18]

$$M_{\lambda\mu} = \sum_{j=1}^{A}\left[\frac{2}{\lambda+1}g_l^j \boldsymbol{l}_j + g_s^j \boldsymbol{s}_j\right]\cdot\nabla_j \ \ [r_j^\lambda Y_{\lambda\mu}(\hat{r}_j)], \tag{12}$$

where λ is the rank of the tensor operator [19], while $\boldsymbol{l}_j$ and $\boldsymbol{s}_j$ are the orbital and intrinsic angular momenta of the j-th nucleon, respectively. The values of g factors are taken from [18]. With the free-space bare operators (12) being renormalized into the valence-space using the $\hat{\Theta}$ box, we can get the expectation of the operator, i.e. $\langle\psi_f\|\boldsymbol{M}\lambda\|\ \psi_i\rangle$, with ψ_i and ψ_f being the wave functions of the initial and final state.

In this work, our main concerns are the magnetic moment and the reduced transition probability.

The magnetic moment of the state $|\psi_J\rangle$ is defined as

$$\mu = \sqrt{\frac{4\pi}{3}}\sqrt{\frac{J}{(J+1)(2J+1)}}\langle\psi_J\|\boldsymbol{M}1\|\psi_J\rangle, \tag{13}$$

with J being the total angular momentum of the state $|\psi_J\rangle$. For extreme single-particle or single-hole condition, the value of magnetic moment, also known as the Schmidt limit [20], can be obtained from the following equation,

$$\mu_{\rm sp} = \begin{cases} g_l j + \frac{1}{2}(g_s - g_l) & \text{for } j = l + \frac{1}{2}, \\ g_l j - (g_s - g_l)\frac{j}{2j+2} & \text{for } j = l - \frac{1}{2}, \end{cases} \tag{14}$$

where j and l represent the total angular momentum and orbital angular momentum of the orbit of the single particle or single hole, g_l and g_s are the free-nucleon g-factors [18].

The reduced transition probability is defined as

$$B(\boldsymbol{M}\lambda;\ \psi_i \to \psi_f) = \frac{1}{2J_i+1}|\langle\psi_f\|\boldsymbol{M}\lambda\|\psi_i\rangle|^2, \tag{15}$$

with J_i being the angular momentum of the initial state. The transition probability can be calculated using

$$T_{i\to f}^{(\boldsymbol{M}\lambda)} = \frac{2}{\epsilon_0\hbar}\frac{\lambda+1}{\lambda[(2\lambda+1)!!]^2}\left(\frac{E_\gamma}{\hbar c}\right)^{2\lambda+1}B(\boldsymbol{M}\lambda;\ \psi_i \to \psi_f), \tag{16}$$

where E_γ is the γ-decay energy from the state ψ_i to the state ψ_f in units of MeV. ϵ_0 and $\hbar c$ are physics constants [18]. The partial half-life of the decay from ψ_i to ψ_f is calculated by

$$t_{1/2}^{i\to f} = \frac{\ln 2}{T_{i\to f}}. \tag{17}$$

2.2.2. β decay. The full-space bare Fermi (F) and Gamow–Teller (GT) β decay operator are defined as [21]

$$O(F) = \sum_j^A \tau_\pm^j, \quad O(GT) = \sum_j^A \sigma^j\tau_\pm^j, \tag{18}$$

where σ stands for the Pauli spin operator and $\tau_\pm$ are isospin operators corresponding to $\beta^\pm$ decays, respectively. We can then get the reduced F or GT transition matrix element [21] by

$$M_{\rm F} = \delta_{J_iJ_f}\sum_{p,q} M_{\rm F}^{p,q}\langle\psi_f\|[a_p^\dagger a_q]\|\psi_i\rangle, \tag{19}$$

and

$$M_{\rm GT} = \sum_{p,q} M_{\rm GT}^{p,q}\langle\psi_f\|[a_p^\dagger a_q]\|\psi_i\rangle. \tag{20}$$

where J_i (J_f) is the angular momentum of the initial (final) state. p and q runs over all the index in the valence-space. It should be noted that for β^- decay p must be proton index and q must be neutron index, while for β^+ decay and electron capture (EC) the situation is opposite. $M_{\rm F}^{p,q}$ and $M_{\rm GT}^{p,q}$ are the valence-space effective F and GT transition matrix elements, respectively, derived from the full-space F and GT operator through the $\hat{\Theta}$-box calculations.

With the value of $M_{\rm F}$ and $M_{\rm GT}$, we can calculate the F and GT reduced transition probabilities,

$$B_{\rm F} = \frac{g_{\rm V}^2}{2J_i+1}|M_{\rm F}|^2, \quad B_{\rm GT} = \frac{g_{\rm A}^2}{2J_i+1}|M_{\rm GT}|^2, \tag{21}$$

where J_i is the angular momentum of the initial state, while the factor $g_{\rm V}$ and $g_{\rm A}$ are the vector coupling constant of the weak interactions and the axial-vector coupling constant of the weak interactions [18], respectively. The half-life of the β decay from the initial state i to a final state f can be calculated by

$$t_{1/2}^{i\to f} = \frac{\kappa}{f(B_{\rm F}+B_{\rm GT})}. \tag{22}$$

where the constant $\kappa = 6289$ s [22], f is the phase factor [18].

2.2.3. Half-life. Within the equations above, we can calculate the half-life of an initial state i by

$$\frac{1}{t_{1/2}^{\rm total}} = \sum_f \frac{1}{t_{1/2}^{i\to f}} \tag{23}$$

where the sum runs over all the decay branches, including the electromagnetic transitions and β decays.

3. Results and discussion

In the present work, we used the NN+3N$_{\rm lnl}$ [23, 24] with the NN interaction at N^{4}LO [25] and the 3N interaction, which has the low-energy constants $c_D = -1.80$, $c_E = -0.31$ [23] and uses a mixture of local and non-local regulators [23, 24], as our input interaction. To speed up convergence, the NN and 3N interactions were consistently SRG evolved to the

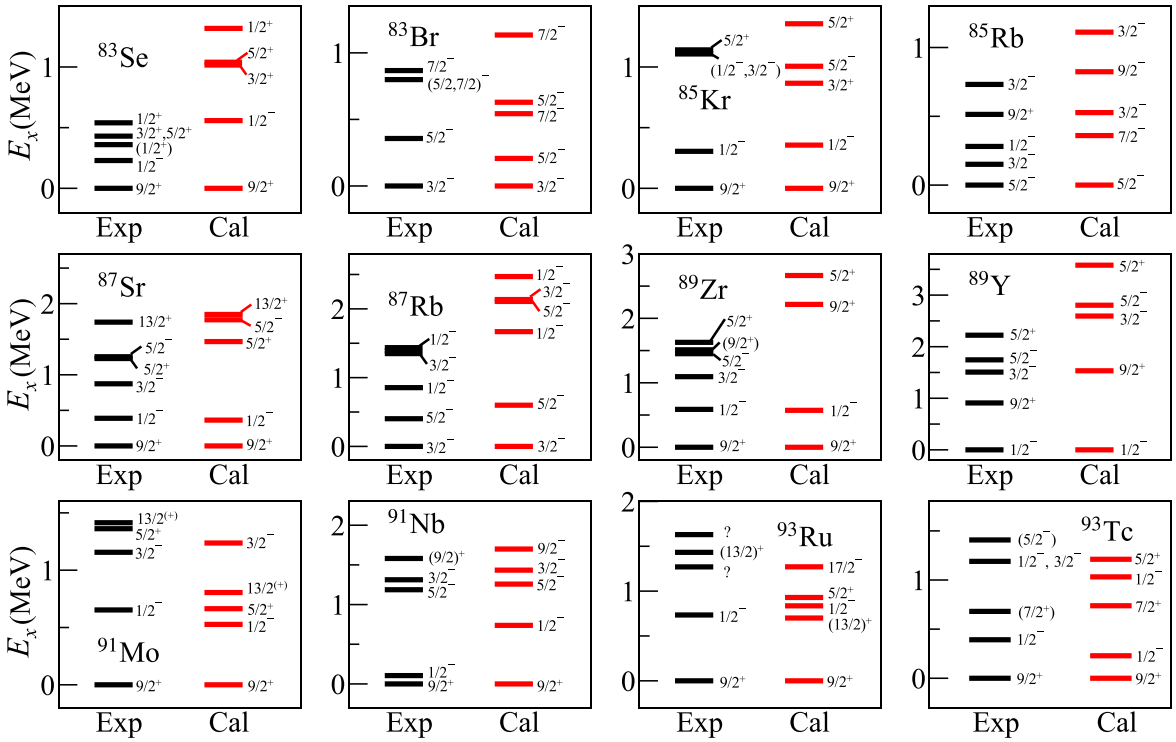

Figure 1. Spectra of $N = 49$ isotones and their daughter nuclei. Experimental data ara taken from [35]. The NN+3N$_{\rm lnl}$ interaction were used in the calculation.

lower cutoff $\lambda_{\rm SRG} = 2.0\,{\rm fm}^{-1}$. This interaction can well reproduce the properties from light to medium-mass nuclei [23, 24, 26]. Additionally, the low-energy constants c_D and c_E in 3N force of the NN+3N$_{\rm lnl}$ interaction are constrained to the triton half-life and binding energy [23]. In [23] and [27], calculations using NN+3N$_{\rm lnl}$ can give better GT strength and $B(M5)$ than using other forces, which would indicate that considering triton half-life would make the nuclear force better describe spin-dependent or isomorphic spin-dependent operators. The HO basis at $\hbar\omega = 16$MeV with $e = 2n + l \leqslant e_{\rm max} = 14$ was taken in our calculations, and we limited $e_1 + e_2 + e_3 \leqslant E_{3\rm max} = 24$ for 3NF. In [28], it has been demonstrated that the calculation with $e_{\rm max} = 14$ and $E_{3\rm max} = 24$ can reach convergence for energies and other operators.

Using the MBPT, we have derived an effective shell-model Hamiltonian with the $\pi(f_{5/2},\ p_{3/2},\ p_{1/2},\ g_{9/2}) \otimes \nu(p_{1/2},\ g_{9/2},\ g_{7/2},\ d_{5/2})$ valence-space above ^{66}Ni core for shell-model calculations. The shell-model calculation was performed using the large-scale shell-model code KSHELL [29]. As the large dimensions of the valence-space exceed the computational capacity of the supercomputer and the neutron excitations across $N = 50$ shell has been demonstrated to be very little in the low-lying states of the nuclei in this region in previous phenomenological shell-model calculations [30–34], we implement the truncation, which allows the valence protons to move freely among all the valence-proton orbits and a total of up to two neutrons to fill in the $\nu(g_{7/2},\ d_{5/2})$ orbits, in this work.

The spectra of $N = 49$ isotones and their daughter nuclei are given in figure 1. As can be seen in figure 1, we well reproduce the spectra of these nuclei. In [36], Cai has demonstrated that the $1/2^-$ states in $N = 50$ isotones raise from the excitation of a single unpaired proton hole from $\pi 1p_{1/2}$ to $\pi 0g_{9/2}$. To illustrate the origin of $1/2^-$ states in $N = 49$ isotones, we show the configurations of $9/2^+$ ground states and $1/2^-$ states in these nuclei, as show in figure 2. In figure 2, we can find that a nuetron excite from $\nu 1p_{1/2}$ to $\nu 0g_{9/2}$ when nuclei excite from $9/2^+$ states to $1/2^-$ states. However, the configurations are different between $9/2^+$ and $1/2^-$ states in ^{83}Se compared with other nuclei, as shown in figure 2(a), and this would be the origin the difference between the experimental and theoretical energy values of the $1/2^-$ state of ^{83}Se. From figure 2(a), we can find that as the number of protons increases, the valence protons gradually fill the $\pi 0f_{5/2}$, $\pi 1p_{3/2}$ and $\pi 1p_{1/2}$ orbits. The excitation on $\pi 0g_{9/2}$ orbit is the reason that magnetic moment of ^{89}Zr deviate single-particle value. If we restrict the excitations on $\pi 0g_{9/2}$ orbit, theoretical magnetic moment of ^{89}Zr is 0.613 $\mu_{\rm N}$, which is close to the Schmidt limit, 0.638 $\mu_{\rm N}$.

Since these $1/2^-$ states of these nuclei can be considered to be caused by the excitation of a single unpaired neutron hole from $\nu 1p_{1/2}$ to $\nu 0g_{9/2}$, the states should have strong single-particle phenomena. To reveal this single-particle picture of $1/2^-$ states, we have calculated the magnetic moment of them compared with experimental data [35] and the extreme single-particle magnetic moment of a neutron on the $\nu p_{1/2}$ orbit which is the so-called 'Schmidt limit' [20], as can be seen in figure 3.

In figure 3, it can be found that our calculation well reproduce the experimental data. The magnetic moments of ^{83}Se, ^{85}Kr and ^{87}Sr are very close to the single-particle value,

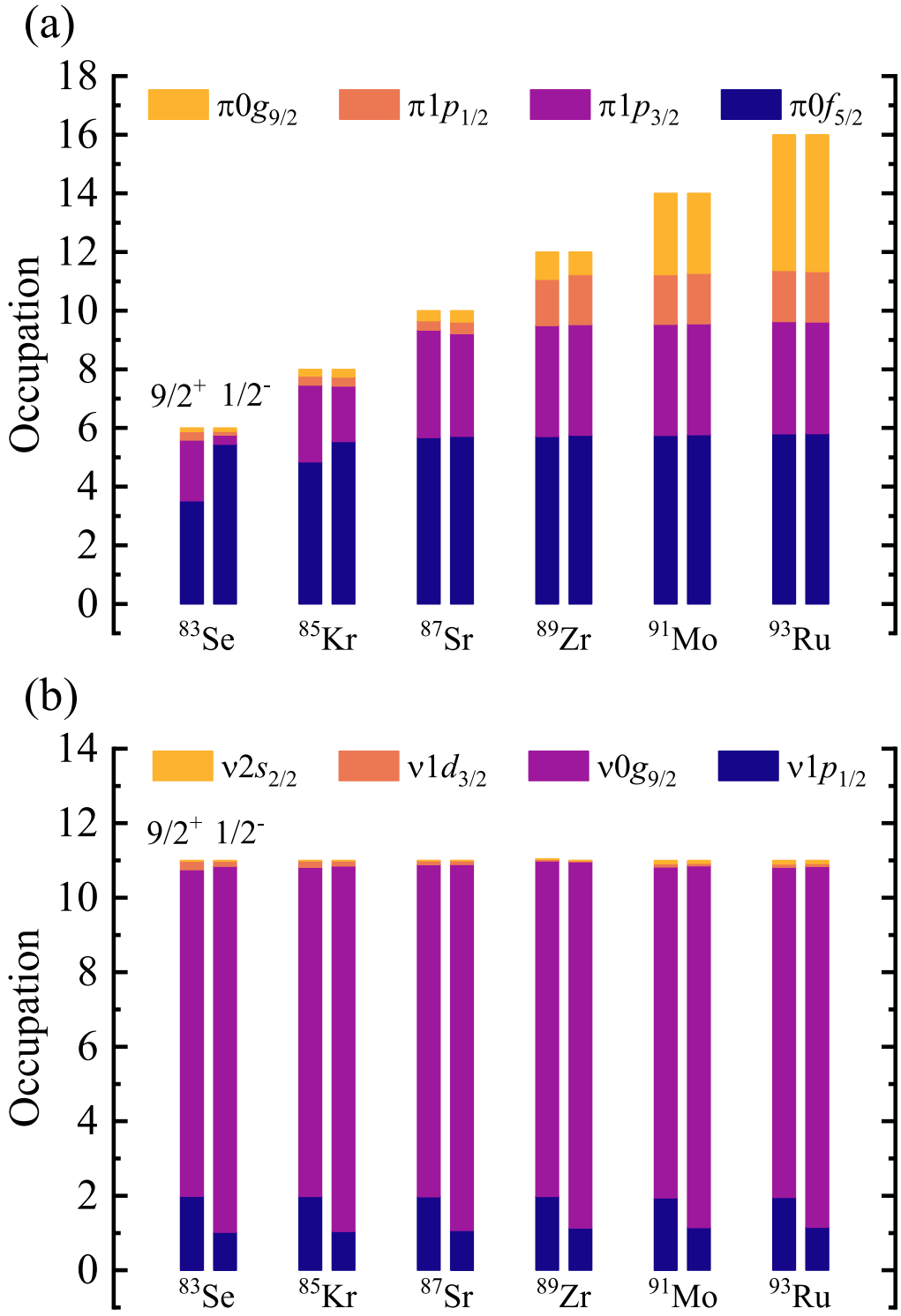

Figure 2. Configurations of $9/2^+$ states and $1/2^-$ states in $N = 49$ isotones for proton orbits (a) and neutron orbits (b) in the valence-space.

which reveal the robust single-particle characteristics in these three nuclei. However, for ^{89}Zr, ^{91}Mo and ^{93}Ru, the values of the magnetic moments deviates slightly from the Schmidt limit for both experimental data and computational results. Our calculations also indicate that the magnetic moments of the $1/2^-$ isomeric states in ^{91}Mo and ^{93}Ru are almost the same and both of them are slightly smaller than that of ^{89}Zr.

To deeply understand the $1/2^-$ states, we have also studied the decay properties of these states. We firstly calculated the reduced transition probabilities of the observed $M4$ transition of the $1/2^-$ isomeric states, which is listed on table 1, compared with the experimental data. As can be found in figure 3, the calculated $M4$ reduced transition probabilities differs from the experimental data about 1.5 to 3

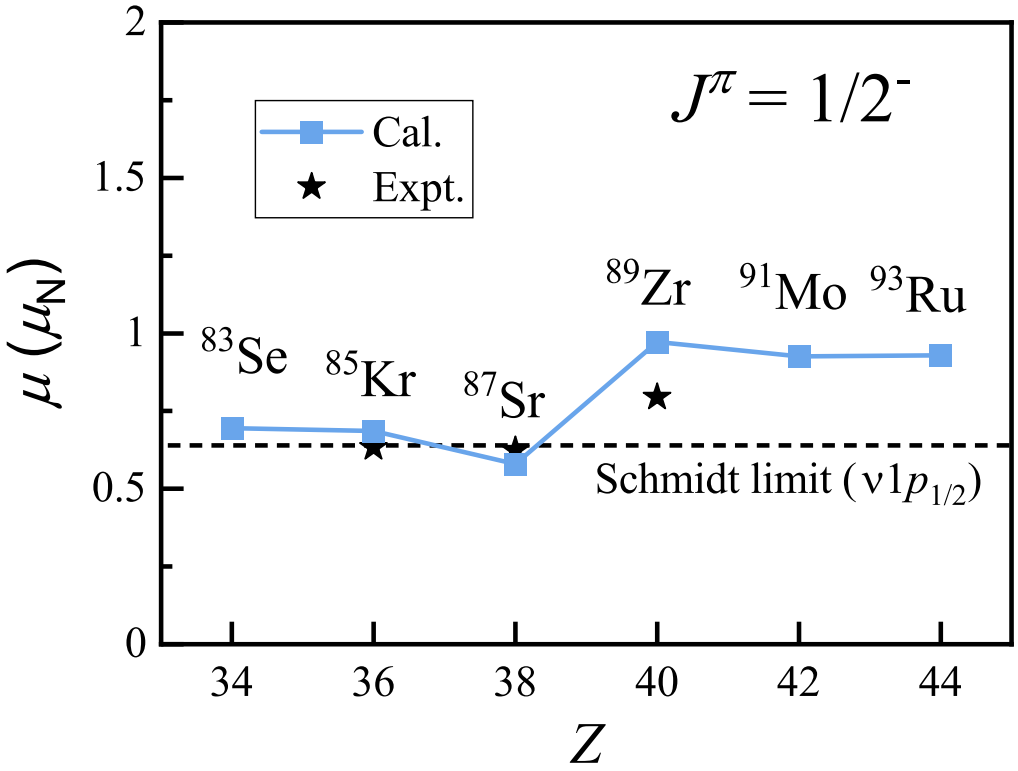

Figure 3. Nuclear magnetic moments for the $1/2^-$ isomeric states of $N = 49$ isotones, compared with experimental data [35]. The horizontal dotted line means the single-particle value (Schmidt limit).

Table 1. Calculated reduced transition probabilities $B(M4)$ of the $1/2^-$ isomers observed in $N = 49$ isotones in units of $10^5\mu_N^2\,\mathrm{fm}^6$. The NN+3N$_{\mathrm{lnl}}$ potentials are used. The experimental data is taken from [35].

Nucleus	Transition	$B(M4)$ $(10^5\mu_N^2\,\mathrm{fm}^6)$	
		Cal.	Expt.
^{85}Kr	$\frac{1}{2}^- \rightarrow \frac{9}{2}^+$	2.54	1.41(4)
^{87}Sr		3.93	1.49(1)
^{89}Zr		4.41	1.58(1)
^{91}Mo		3.41	1.27(4)
^{93}Ru		2.77	1.18(14)

times. In addition to $M4$ magnetic transition, the $1/2^-$ isomeric states can also decay through β transition.

Tables 2 and 3 give the theoretical results of Fermi and Gamow–Teller reduced transition probabilities, along with computational and experimental logft values of all the observed β-decay branch of the $1/2^-$ isomeric states which we studied. It should be noted that due to the selection rules for allowed beta decay transitions, the values of $B(F)$ are theoretically equal to zero when the J^π of the final state is $3/2^-$. The Fermi operator connects isobaric analog states [37], which means that the initial state and final state of a β decay can been seen as isobaric analog states with each other if $B(F)$ is much larger than $B(GT)$. As can be seen in the two tables, we can find that, for those branches whose final states are $J^\pi = 1/2^-$ on experiment, our calculations give $B(GT)$ values that are bigger than $B(F)$, which means that these states are isospin-mixed states and the isobaric analog component are smaller than the isobaric non-analog component. However, for the branches whose final states are degenerate with J^π being $1/2^-$ and $3/2^-$ on experiment, except for two branches of ^{83m}Se with the final states being ^{83}Br $\left(\frac{1}{2_2}^-, \frac{3}{2_3}^-\right)$ and ^{83}Br $\left(\frac{1}{2_4}^-, \frac{3}{2_6}^-\right)$ on experiment, our calculations give similar $B(F)$ and $B(GT)$ values for the final state with $J^\pi = 1/2^-$ on theory, which indicates that the proportions of the isobaric analog component and isobaric non-analog component are similar in these states. Additionally, our results show that the decay branches of ^{83m}Se, whose the final states are ^{83}Br $\left(\frac{1}{2_2}^-, \frac{3}{2_3}^-\right)$ and ^{83}Br $\left(\frac{1}{2_4}^-, \frac{3}{2_6}^-\right)$ on experiment, have strong $B(F)$ values compared with $B(GT)$ for the final state with $J^\pi = 1/2^-$ on theory, which can be seen in

Table 2. Calculated β-decay reduced transition probabilities and calculated and experimental logft values of the $1/2^-$ isomers observed in ^{83}Se, ^{85}Kr and ^{87}Sr. The NN+3N$_{\rm lnl}$ potentials are used. The experimental data is taken from [35].

Transition			$B(F)$	$B(GT)$	logft	
Initial(J^π)	Final(J^π)					
	Expt.	Cal.			Expt.	Cal.
^{83}Se($\frac{1}{2_1}^-$)	^{83}Br($\frac{3}{2_1}^-$)	^{83}Br($\frac{3}{2_1}^-$)	0	7.29×10^{-4}	6.0(1)	6.9
	^{83}Br($\frac{1}{2_2}^-$, $\frac{3}{2_3}^-$)	^{83}Br($\frac{1}{2_2}^-$)	2.79×10^{-2}	4.12×10^{-4}	5.8(1)	5.3
		^{83}Br($\frac{3}{2_3}^-$)	0	1.42×10^{-2}		5.6
	^{83}Br($(\frac{3}{2})_4^-$)	^{83}Br($\frac{3}{2_4}^-$)	0	2.30×10^{-3}	5.4(1)	6.4
	^{83}Br($\frac{1}{2_3}^-$, $\frac{3}{2_5}^-$)	^{83}Br($\frac{1}{2_3}^-$)	2.31×10^{-4}	5.76×10^{-4}	7.3(1)	6.9
		^{83}Br($\frac{3}{2_5}^-$)	0	3.33×10^{-3}		6.3
	^{83}Br($\frac{1}{2_4}^-$, $\frac{3}{2_6}^-$)	^{83}Br($\frac{1}{2_4}^-$)	2.72×10^{-5}	4.25×10^{-7}	6.0(1)	8.4
		^{83}Br($\frac{3}{2_6}^-$)	0	1.12×10^{-2}		5.7
	^{83}Br($\frac{1}{2_5}^{(-)}$, $\frac{3}{2_8}$)	^{83}Br($\frac{1}{2_5}^-$)	2.41×10^{-4}	5.99×10^{-4}	5.9(1)	6.9
		^{83}Br($\frac{3}{2_8}^-$)	0	2.76×10^{-4}		7.4
	^{83}Br($\frac{1}{2_6}^-$, $\frac{3}{2_9}^-$)	^{83}Br($\frac{1}{2_6}^-$)	1.36×10^{-3}	2.51×10^{-3}	4.8(1)	6.2
		^{83}Br($\frac{3}{2_9}^-$)	0	1.86×10^{-2}		5.5
	^{83}Br($\frac{1}{2_{10}}^-$, $\frac{3}{2_{13}}^-$)	^{83}Br($\frac{1}{2_{10}}^-$)	8.28×10^{-3}	8.75×10^{-3}	5.9(4)	5.6
		^{83}Br($\frac{3}{2_{13}}^-$)	0	2.75×10^{-3}		6.4
	^{83}Br($\frac{1}{2_{11}}^-$, $\frac{3}{2_{14}}^-$)	^{83}Br($\frac{1}{2_{11}}^-$)	3.60×10^{-2}	4.40×10^{-2}	5.7(1)	4.9
		^{83}Br($\frac{3}{2_{14}}^-$)	0	8.53×10^{-2}		4.9
^{85}Kr($\frac{1}{2_1}^-$)	^{85}Rb($\frac{3}{2_1}^-$)	^{85}Rb($\frac{3}{2_1}^-$)	0	5.71×10^{-2}	7.1(1)	5.042
	^{85}Rb($\frac{1}{2_1}^-$)	^{85}Rb($\frac{1}{2_1}^-$)	4.17×10^{-5}	6.51×10^{-4}	7.39(2)	6.96
	^{85}Rb($\frac{3}{2_2}^-$)	^{85}Rb($\frac{3}{2_2}^-$)	0	2.98×10^{-5}	5.250(8)	8.325
^{87}Sr($\frac{1}{2_1}^-$)	^{87}Rb($\frac{3}{2_1}^-$)	^{87}Rb($\frac{3}{2_1}^-$)	0	1.51	4.40(12)	3.62

table 2, demonstrating strong isobaric analog component in these two decay branches.

With the values in tables 1, 2 and 3, we also calculated the half-life of these $1/2^-$ isomers using equation (17), (22) and (23), which are given in table 4. Because the calculation result of half-life is very sensitive to the electromagnetic transition energy E_γ and Q values of β decay, we use the experimental value [35] in the half-life calculation. It can be seen from table 4 that our calculations and experimental results are in very good agreement, showing the reliability of *ab initio* calculations in description of spin isomers.

4. Summary

We have performed *ab initio* calculations for the $N = 49$ isotones. We have derived the valence-space effective Hamiltonian and other effective operators with the chiral two- plus three-nucleon force NN+3N$_{lnl}$ using the $\hat{Q}$-box and $\hat{\Theta}$-box folded diagrams, respectively, with the ^{66}Ni core. With the valence-space effective Hamiltonian and operators, we have investigated the magnetic moments and the decay properties of isomers of the $N = 49$ isotones.

We first calculate the energies and the magnetic moments of the $1/2^-$ isomers o $N = 49$ isotones. Our calculations reproduce reasonably experimental data and revealed the strong single-particle phenomena in ^{83}Se, ^{85}Kr and ^{87}Sr. We then focus on the decay properties of the isomers we studied, including $M4$ magnetic transitions and β-decay properties. Our calculations can give good results of these properties, demonstrating the reliability of *ab initio* theory of studying the structure and decay properties of spin isomers in $A \approx 90$ mass region.

Table 3. Same as table 2 but for $1/2^-$ isomers in ^{89}Zr, ^{91}Mo and ^{93}Ru.

Initial(J^π)	Transition Final(J^π) Expt.	Transition Final(J^π) Cal.	$B(F)$	$B(GT)$	log ft Expt.	log ft Cal.
^{89}Zr$\left(\frac{1}{2_1}^-\right)$	^{89}Y$\left(\frac{1}{2_1}^-\right)$	^{89}Y$\left(\frac{1}{2_1}^-\right)$	1.23×10^{-2}	3.36×10^{-2}	7.1(4)	5.1
	^{89}Y$\left(\frac{3}{2_1}^-\right)$	^{89}Y$\left(\frac{3}{2_1}^-\right)$	0	1.63	4.31(2)	3.59
^{91}Mo$\left(\frac{1}{2_1}^-\right)$	^{91}Nb$\left(\frac{1}{2_1}^-\right)$	^{91}Nb$\left(\frac{1}{2_1}^-\right)$	7.56×10^{-3}	2.88×10^{-2}	5.94(22)	1.27(4)
	^{91}Nb$\left(\frac{3}{2_1}^-\right)$	^{91}Nb$\left(\frac{3}{2_1}^-\right)$	0	3.31×10^{-3}	4.78(4)	
	^{91}Nb$\left(\frac{3}{2_2}^-\right)$	^{91}Nb$\left(\frac{3}{2_2}^-\right)$	0	1.54	4.4(4)	
	^{91}Nb$\left(\left(\frac{3}{2}\right)_3^-\right)$	^{91}Nb$\left(\frac{3}{2_3}^-\right)$	0	5.11×10^{-3}	5.03(4)	
^{93}Ru$\left(\frac{1}{2_1}^-\right)$	^{93}Tc$\left(\frac{1}{2_1}^-\right)$	^{93}Tc$\left(\frac{1}{2_1}^-\right)$	1.27×10^{-2}	3.93×10^{-2}	>5.6	5.1
	^{93}Tc$\left(\frac{1}{2_3}^-, \frac{3}{2_2}^-\right)$	^{93}Tc$\left(\frac{1}{2_3}^-\right)$	1.20×10^{-2}	1.05×10^{-2}	4.84(3)	5.45
		^{93}Tc$\left(\frac{3}{2_2}^-\right)$	0	2.28×10^{-3}		6.44
	^{93}Tc$\left(\frac{1}{2_4}^-, \frac{3}{2_3}^-\right)$	^{93}Tc$\left(\frac{1}{2_4}^-\right)$	9.29×10^{-3}	2.93×10^{-3}	4.526(19)	5.712
		^{93}Tc$\left(\frac{3}{2_3}^-\right)$	0	1.38		3.658
	^{93}Tc$\left(\left(\frac{1}{2_5}, \frac{3}{2_4}\right)^-\right)$	^{93}Tc$\left(\frac{1}{2_4}^-\right)$	1.75×10^{-2}	3.51×10^{-3}	4.72(3)	5.48
		^{93}Tc$\left(\frac{3}{2_4}^-\right)$	0	3.16×10^{-2}		5.30
	^{93}Tc$\left(\left(\frac{3}{2}\right)_5^-\right)$	^{93}Tc$\left(\frac{3}{2_5}^-\right)$	0	2.06×10^{-3}	⩽4.7	6.5

Table 4. Calculated half-life of the $1/2^-$ isomers in $N = 49$ isotones, compared with experimental [35].

Nucleus	half-life Cal.	half-life Expt.
^{83}Se	2.74 min	1.17(1) min
^{85}Kr	6.197 h	4.480(8) h
^{87}Sr	3.645 h	2.815(12) h
^{89}Zr	32.638 min	4.161(12) min
^{91}Mo	76.1 s	65.0(7) s
^{93}Ru	7.4 s	10.8(3) s

Acknowledgments

This work has been supported by the National Key R&D Program of China under Grant Nos. 2024YFA1610900 and 2023YFA1606401; the National Natural Science Foundation of China under Grant Nos. 12335007 and 12035001. We acknowledge the High-Performance Computing Platform of Peking University for providing computational resources.

References

[1] Walker P and Podolyák Z 2020 100 years of nuclear isomers —then and now *Phys. Scr.* **95** 044004
[2] Garg S, Maheshwari B, Singh B, Sun Y, Goel A and Jain A K 2023 Atlas of nuclear isomers—second edition *At. Data Nucl. Data Tables* **150** 101546
[3] Hergert H 2020 A guided tour of *ab initio* nuclear many-body theory *Front. Phys.* **8** 379
[4] Hu B S *et al* 2022 *Ab initio* predictions link the neutron skin of ^{208}Pb to nuclear forces *Nat. Phys.* **18** 1196–200
[5] Xu X Y, Fan S Q, Yuan Q, Hu B S, Li J G, Wang S M and Xu F R 2024 Progress in *ab initio* in-medium similarity renormalization group and coupled-channel method with coupling to the continuum *Nucl. Sci. Tech.* **35** 215
[6] Ye Y L, Yang X F, Sakurai H and Hu B S 2024 Physics of exotic nuclei *Nat. Rev. Phys.* **7** 21–37
[7] Machleidt R and Entem D 2011 Chiral effective field theory and nuclear forces *Phys. Rep.* **503** 1–75
[8] Coraggio L and Itaco N 2020 Perturbative approach to effective shell-model Hamiltonians and operators *Frontiers in Physics* **8** 1–23
[9] Stroberg S R, Holt J D, Schwenk A and Simonis J 2021 *Ab initio* limits of atomic nuclei *Phys. Rev. Lett.* **126** 022501
[10] Zhang S, Xu F R, Li J G, Hu B S, Cheng Z H, Michel N, Ma Y Z, Yuan Q and Zhang Y H 2023 *Ab initio* descriptions of $A = 16$ mirror nuclei with resonance and continuum coupling *Phys. Rev.* C **108** 064316
[11] Zhang S, Ma Y, Li J, Hu B, Yuan Q, Cheng Z and Xu F 2022 The roles of three-nucleon force and continuum coupling in mirror symmetry breaking of oxygen mass region *Phys. Lett.* B **827** 136958
[12] Xu Z C, Zhang S, Li J G, Jin S L, Yuan Q, Cheng Z H, Michel N and Xu F R 2023 Complex valence-space effective operators for observables: the Gamow–Teller transition *Phys. Rev.* C **108** L031301

[13] Sun Z, Wu Q, Zhao Z, Hu B, Dai S and Xu F 2017 Resonance and continuum Gamow shell model with realistic nuclear forces *Phys. Lett.* B **769** 227–32
[14] Takayanagi K 2011 Effective interaction in non-degenerate model space *Nucl. Phys.* A **852** 61–81
[15] Tsunoda N, Takayanagi K, Hjorth-Jensen M and Otsuka T 2014 Multi-shell effective interactions *Phys. Rev.* C **89** 024313
[16] Coraggio L and Itaco N 2005 Self-consistent nuclear shell-model calculation starting from a realistic *NN* potential *Phys. Lett.* B **616** 43–7
[17] Suzuki K and Okamoto R 1995 Effective operators in time-independent approach *Prog. Theor. Phys.* **93** 905–17
[18] Suhonen J 2013 *From Nucleons to Nucleus. Concepts of Microscopic Nuclear Theory* (Springer)
[19] Parzuchowski N M, Stroberg S R, Navrátil P, Hergert H and Bogner S K 2017 *Ab initio* electromagnetic observables with the in-medium similarity renormalization group *Phys. Rev.* C **96** 034324
[20] Schmidt T 1937 Über die magnetischen momente der atomkerne *Zeitschrift für Physik* **106** 358–61
[21] Brown B and Wildenthal B 1985 Experimental and theoretical Gamow–Teller beta-decay observables for the *sd*-shell nuclei *At. Data Nucl. Data Tables* **33** 347–404
[22] Patrignani C *et al* (Particle Data Group) 2016 Review of particle physics *Chin. Phys.* C **40** 100001
[23] Gysbers P *et al* 2019 Discrepancy between experimental and theoretical β-decay rates resolved from first principles *Nat. Phys.* **15** 428
[24] Somà V, Navrátil P, Raimondi F, Barbieri C and Duguet T 2020 Novel chiral Hamiltonian and observables in light and medium-mass nuclei *Phys. Rev.* C **101** 014318
[25] Entem D R, Machleidt R and Nosyk Y 2017 High-quality two-nucleon potentials up to fifth order of the chiral expansion *Phys. Rev.* C **96** 024004
[26] Leistenschneider E *et al* 2018 Dawning of the $N = 32$ shell closure seen through precision mass measurements of neutron-rich titanium isotopes *Phys. Rev. Lett.* **120** 062503
[27] Fan S Q, Yuan Q, Xu F R and Walker P *Ab initio* studies of the highest-multipole electromagnetic transition ever observed in atomic nuclei *Nucl. Sci. Tech.* Accepted
[28] Belley A, Miyagi T, Stroberg S R and Holt J D 2023 *Ab initio* calculations of neutrinoless decay refine neutrino mass limits arXiv: 2307.15156
[29] Shimizu N, Mizusaki T, Utsuno Y and Tsunoda Y 2019 Thick-restart block Lanczos method for large-scale shell-model calculations *Comput. Phys. Commun.* **244** 372–84
[30] Luo P W *et al* 2014 High-spin level structure of the semi-magic nucleus ^{91}Nb *Phys. Rev.* C **89** 034318
[31] Zheng Y *et al* 2019 Reinvestigation of the high-spin level structure of ^{92}Nb: excitations across the $Z = 38$ and $N = 50$ closed shells *Phys. Rev.* C **100** 014325
[32] Dey P *et al* 2022 Experimental investigation of high-spin states in ^{90}Zr *Phys. Rev.* C **105** 044307
[33] Wu Y H *et al* 2024 Experimental study of the level structure in ^{90}Nb and systematics of level structure characteristics near $A = 90$ *Phys. Rev.* C **109** 024326
[34] Pattabiraman N S, Chintalapudi S N, Ghugre S S, Tirumala Rao B V, Raju M L N, Reddy T S, Joshi P K, Palit R and Jain H C 2002 Level structure of ^{92}Mo at high angular momentum: evidence for $Z = 38$, $N = 50$ core excitation *Phys. Rev.* C **65** 044324
[35] National Nuclear Data Center https://www.nndc.bnl.gov/ensdf/
[36] Cai B, Yuan C, Zhang G, Zhang Y, Liu M, Xing Y, Xu X, Li J and Wang M 2024 Isomeric structure in the ^{100}Sn region: possible competition between β^+ decay and proton emission in the isomeric unbound nucleus ^{97}Sn *Phys. Rev.* C **109** L051302
[37] Brown B A 2005 *Lecture Notes in Nuclear Structure Physics* https://inpp.ohio.edu/~meisel/PHYS7501/file/BAB-lecture-notes.pdf